ELSEVIER

Contents lists available at ScienceDirect

Journal of Power Sources

journal homepage: www.elsevier.com/locate/jpowsour





Fluorinated ether decomposition in localized high concentration electrolytes

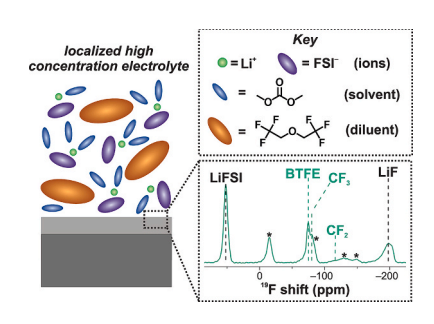
Richard May^a, Julia C. Hestenes^b, Naiara A. Munich^c, Lauren E. Marbella^{a,*}

- ^a Department of Chemical Engineering, Columbia University, New York, NY, 10027, USA
- b Program of Materials Science and Engineering, Department of Applied Physics and Applied Mathematics, Columbia University, New York, NY, 10027, USA
- ^c Department of Chemistry, Barnard College, New York, NY, 10027, USA

HIGHLIGHTS

- Operando ¹⁹F NMR tracks fluorinated ether degradation in LHCEs.
- Solid-state NMR identifies electrolyte decomposition products on the Li surface.
- EIS correlates impedance at the electrodes with the resulting surface chemistry.

GRAPHICAL ABSTRACT



ABSTRACT

Localized high concentration electrolytes (LHCEs) are a promising class of battery materials to enable stable cycling of the lithium metal anode. Here, we report the use of *operando* nuclear magnetic resonance (NMR) spectroscopy to observe electrolyte decomposition during Li stripping/plating and identify the influence of individual components in LHCEs on Li metal battery performance. Data from *operando* ¹⁹F solution NMR indicates that both bis(fluorosulfonyl)imide (FSI⁻) salt and bis(2,2,2-trifluoroethyl) ether (BTFE) diluent molecules play a key role in solid electrolyte interphase (SEI) formation. Three-electrode electrochemical impedance spectroscopy (EIS) of commercial pouch cells also shows differences in interfacial resistances between LHCE and standard high concentration electrolytes (HCEs) that may be explained by incorporation of BTFE and BTFE reaction products into the SEI. Based on solid-state NMR and X-ray photoelectron spectroscopic characterization, we find that BTFE diluents decompose to form CF₂- and CF₃-containing fragments within a LiF-rich SEI deposited on the anode surface. The CEI on the cathode (here, LiNi_{0.8}Mn_{0.1}Co_{0.1}O₂) side of the battery also contains higher quantities of LiF and trapped LiFSI after cycling in the LHCE compared to a HCE that are attributed to diluent decomposition and correlated with lower impedance at the cathode. Overall, this work provides a new framework to consider highly fluorinated ether molecules—instead of functioning purely as diluting agents in LHCEs, these fluorinated ethers exhibit tunable interfacial reactivity that can be leveraged to control Li deposition behavior.

1. Introduction

Li metal anodes react with liquid electrolytes to generate a solid electrolyte interphase (SEI) that dictates the stability of Li stripping and plating during battery operation [1–5]. Increasing Li salt concentration

in the electrolyte is a straightforward way to produce smooth Li deposits and high coulombic efficiency (CE) values [6-10] to potentially realize high performance Li metal batteries. A larger ratio of Li salt to solvent results in a deficit of solvent molecules that can no longer fully coordinate Li⁺ cations, leading to the formation of contact-ion pairs [6,11].

E-mail address: lem2221@columbia.edu (L.E. Marbella).

https://doi.org/10.1016/j.jpowsour.2022.232299

^{*} Corresponding author.

High salt concentration electrolytes (HCEs) lower the energy level of the lowest unoccupied molecular orbital (LUMO) of the salt anions, which leads to preferential reduction of the anions over the solvent molecules, eventually forming inorganic-rich SEI chemistries [12,13]. For example, increasing the salt concentration from ~ 1 M to ~ 4 M in Li bis(fluorosulfonyl)imide (LiFSI) dissolved in dimethyl carbonate (DMC) shifts the LUMO from DMC to FSI $^-$ [14,15]. As a result, preferential reduction of FSI $^-$ at high salt concentration forms a predominantly inorganic SEI that is believed to passivate the Li metal surface and stabilize Li stripping/plating processes [9,11,16].

Unfortunately, HCEs are impractical due to low ionic conductivities (from high viscosities) and high costs associated with increasing the salt content in the electrolyte. In contrast, localized high concentration electrolytes (LHCEs) offer a route to circumvent these problems by using a diluent (typically a fluorinated ether) to lower the nominal salt concentration. The lower nominal salt concentration has the potential to lower the overall cost of the electrolyte (given that LiFSI salts are expensive) as well as the viscosity of the solution (since electrolyte viscosity is directly correlated with salt concentration). The diluent in LHCEs does not solvate Li ions, allowing the electrolyte to retain the desirable solvation structures found at high salt concentration (e.g., contact-ion pairs) [17-19]. LHCEs are reported to form microscopic phases of HCE that exist separately from the bulk diluent (here, bis(2,2, 2-trifluoroethyl) ether (BTFE)) [17,20], decoupling the interfacial properties (that are dictated by the immediate environment of Li⁺) from the bulk properties (which are modulated by the overall electrolyte composition) of the electrolyte. At present, the impact of small molecule diluents on Li metal battery performance is not entirely clear, as these species may simply mimic the bulk solvation structure of HCEs, allowing the formation of an inorganic-rich SEI while not participating in the decomposition process themselves [18], or alternatively, they may be actively involved in creating a stable SEI [17]. For example, if the diluent molecules do not decompose, the SEI would contain large quantities of LiF from ${\rm FSI}^-$ reduction based on the similarity in solvation structure between LCHEs and HCEs [18]. If the diluent molecules do decompose, we expect that the composition of the resulting SEI would depend on the molecular structure of said diluent (given that the reduction potential is related to the electronic structure). Recent work from Balbuena and coworkers showed that at high diluent concentration, fluorinated ether molecules may undergo nucleophilic attack from F⁻ and get incorporated in the SEI as unsaturated organic fragments [15]. Likewise, Zhang and coworkers reported that the LHCE diluent, 1, 1,2,2-tetrafluoroethyl-2,2,3,3-tetrafluoropropyl ether (TTE), thermally decomposes upon extended contact with Li metal, yet its stability during electrochemical cycling is not known [17].

In this work, we examine the decomposition of the fluorinated small molecule diluent, BTFE, in a LHCE composed of 1.2 M lithium bis(fluorosulfonyl)imide (LiFSI) in 1:2 dimethyl carbonate (DMC):BTFE (v/v). We use operando ¹⁹F nuclear magnetic resonance (NMR) spectroscopy to confirm BTFE diluent decomposition within the LHCE during Li stripping/plating. Post mortem solid-state NMR (SSNMR) spectroscopy and X-ray photoelectron spectroscopy (XPS) of Cu electrodes cycled in commercially-available, multilayer pouch cells show that the SEI formed in the LHCE contains similar amounts of LiF as a typical HCE (4 M LiFSI in DMC), but also includes the presence of CF2 and CF3 groups, likely due to diluent decomposition. The cathode electrolyte interphase (CEI) deposited on the $\text{LiNi}_{0.8}\text{Mn}_{0.1}\text{Co}_{0.1}\text{O}_2$ (NMC811) positive electrode also contains increased quantities of fluorinated inorganics when the pouch cells are cycled in the LHCE versus HCE. These changes in interfacial chemistry due to BTFE decomposition are correlated with differences in impedance at both the anode and the cathode measured using threeelectrode electrochemical impedance spectroscopy (EIS), suggesting that LHCE diluents alter ion transport in both the SEI and CEI. Ultimately, these findings indicate that BTFE, and likely other diluent molecules, play an important role in stabilizing both the anode electrolyte and cathode electrolyte interfaces in addition to altering

properties of the bulk electrolyte.

2. Experimental methods

Materials and Methods. Lithium metal ribbon (0.75 mm thick), dimethyl carbonate (DMC, anhydrous, >99%), and potassium bromide (KBr, 99%), were purchased from Sigma Aldrich. Bis(2,2,2trifluoroethyl)ether (BTFE, 99%) was purchased from Synguest Laboratories. Lithium bis(fluorosulfonyl imide) (LiFSI, 99.0%, battery grade) was purchased from Synthonix. Dimethyl sulfoxide-d₆ (DMSO-d₆, 99.9%) was purchased from Cambridge Isotope Laboratories. Both DMSO- d_6 and BTFE were dried under molecular sieves for 48 h in an Arfilled glovebox (<0.1 ppm O₂, <0.5 ppm H₂O) and BTFE was filtered using a 200 nm pore size polytetrafluoroethylene (PTFE) syringe filter prior to use. KBr was dried in vacuo for a week at 100 °C before bringing into an Ar-filled glovebox. Fluorinated ethylene propylene (FEP) NMR tube liners for operando NMR experiments were purchased from Wilmad Labglass, Low-pass radiofrequency (rf) filters, double-shielded electrochemistry wires, a nonmagnetic wire clip, and an rf shield were purchased from NMR Service, GmbH. Copper mesh and nickel tabs with adhesive polymer tape were purchased from MTI Corporation. NMC811 Cu pouch cells were manufactured by Li-FUN Technology (Xinma Industry Zone, Gold Dragon Road, Tianyuan District, Zhuzhou City, Hunan, PRC, 412000) and shipped dry (without electrolyte). Electrolyte was added after placing pouch cells in the glovebox and sealed for analysis.

Electrolyte formulations. Electrolytes of different compositions (1.2 M LiFSI in DMC, i.e., the low concentration electrolyte, LCE; 4 M LiFSI in DMC, i.e., the high concentration electrolyte, HCE; 1.2 M LiFSI in 1:2 DMC:BTFE v/v, i.e., the LHCE) were prepared in an Ar-filled glovebox. The LCE showed 28 ppm $\rm H_2O$, while the LHCE and HCE showed 10 ppm $\rm H_2O$ in Karl Fischer titration.

Solution NMR measurements. Electrolyte samples were prepared by assembling Li|Li symmetric coin cells with glass fiber separators. Electrolyte was then immediately extracted for pristine samples, whereas cycled samples were prepared by cycling the coin cell at 1 mA cm⁻² and 2 h charge/discharge cycles. Electrolyte was extracted by dipping Li electrodes and separator into 1.2 mL DMSO- d_6 , and compressing the separator with clean tweezers to allow the electrolyte to dissolve in the DMSO- d_6 . Electrolyte in DMSO- d_6 solution was then filtered using a 200 nm pore size PTFE syringe filter to remove Li and glass fiber separator. Filtered samples were then sealed in 5 mm air-tight J Young tubes in the glovebox for data acquisition.

All solution NMR experiments were performed on a Bruker Avance III 400 spectrometer equipped with a triple resonance broadband observe (TBO) probehead. All spectra were recorded at T = 300 K. One-dimensional (1D) ¹⁹F (30° single pulse, 2 s recycle delay, 32 scans, internally referenced to FSI⁻ at 51.2 ppm) NMR spectra were recorded on pristine electrolyte samples as well as electrolyte extracted from Li|Li coin cells after cycling. ¹⁷O (90° single pulse, 50 ms recycle delay, between 4096 and 20480 scans, externally referenced to D₂O at 0 ppm) were collected for the pristine electrolytes, as well as the associated solvent mixtures without dissolved salt (e.g., for the LHCE, 1.2 M LiFSI in 1:2 DMC:BTFE v/v and 1:2 DMC:BTFE v/v were tested). The Python package nmrglue [21] was used to extract processed ¹⁷O NMR data from Bruker Topspin 3.6.1 files. Peaks were deconvoluted and fit to Lorentzian lineshapes using a least-squares minimization algorithm with Python library lmfit [22].

 7 Li and 19 F PFG-NMR spectra were collected using a bipolar gradient pulse sequence with gradient strengths varied from 2.5 to 47.5 G cm $^{-1}$ in 16 increments. For 7 Li, the gradient pulse duration (δ) was 4 ms and the time interval between gradient pulses (Δ , the time during which species were allowed to diffuse during the experiment) was 200 ms. For 19 F, δ = 3 ms and Δ = 100 ms. NMR signal intensities were fit to the Stejskal-Tanner equation to obtain diffusion coefficients:

$$I = I_0 e^{-D\gamma^2 G^2 \delta^2 \left(\Delta - \frac{\delta}{3}\right)} \tag{1}$$

where I_0 is the unweighted signal intensity, I is the signal intensity with the gradient applied, γ is the gyromagnetic ratio of the observe nucleus, G is the gradient strength, and D is the diffusion coefficient.

A detailed discussion of the setup used in the *operando* NMR experiments can be found in the Supplementary information as well as Figs. S1 and S2. One dimensional *operando* ¹⁹F NMR measurements were performed using a 30° single pulse, 5 s recycle delay, and 32 scans per experiment, resulting in \sim 3 min per experiment. Simultaneous Coulombic efficiency (CE) measurements were performed at 2 mA cm⁻², with 30 min of Li plating on Cu followed by stripping to 1 V.

Solid-state NMR measurements. Individual samples were prepared by cycling NMC811 | Cu Li-FUN pouch cells for 15 cycles over 200 h for the LHCE and 50 cycles over 75 h for the HCE at C/10 between 4.2 V and 1.5 V at 0.94 MPa of stack pressure. Prior to cycling, 600 μL of a given electrolyte formulation was added to each cell and allowed to soak for 24 h. Cells were disassembled in the discharged state and microstructural Li was removed from the electrode surface using a razor blade, and dried *in vacuo* overnight in a glass vial. Microstructural Li was mixed thoroughly with KBr (5:1 KBr:Li w/w) using a mortar and pestle in the glovebox before packing into a 1.9 mm o.d. ZrO2 rotor to limit electrical connectivity of conductive Li particles and reduce eddy currents [23] while spinning the sample in the NMR magnet.

All SSNMR experiments were performed on a Bruker Avance NEO 600 MHz spectrometer equipped with a 1.9 mm HXY MAS Bruker NMR probehead. All spectra were collected at room temperature. Prior to each set of measurements, the magic-angle was set using KBr. $^{19}\mathrm{F}$ SSNMR experiments were performed using a spin-echo pulse sequence ($\tau=52.5$ $\mu\mathrm{s}$), a 90° pulse length of 2.7 $\mu\mathrm{s}$, a recycle delay of 20 s, and between 2720 and 3072 scans. $^{19}\mathrm{F}$ spectra were externally referenced to LiF at -204 ppm. The Python package nmrglue [21] was used to extract processed $^{19}\mathrm{F}$ NMR data from Bruker Topspin 3.6.1 files. Peaks were deconvoluted and fit to Lorentzian lineshapes using a least-squares minimization algorithm with Python library lmfit [22].

X-ray photoelectron spectroscopy. Samples for XPS were taken from the same cycled Li-FUN cells used for SSNMR analysis described above. Cu and NMC811 electrodes were cut from the cell and triplewashed in DMC (dipped 30 s per wash) to remove residual salts and prevent charging in the XPS. Samples were dried in vacuo overnight to remove residual electrolyte solvent and prevent sample off-gassing in the evacuated XPS chamber. The samples were mounted on XPS stubs inside of the glovebox using carbon tape. Samples were transferred to the XPS sample chamber using an airtight Ar-filled jar, with exposure to atmosphere estimated to be <5 s for each sample. Spectra were collected using a PHI 5600 XPS system with a hemispherical analyzer and an Al Xray source with XPS base chamber pressure $<3.0\times10^{-8}$ Torr. XPS Peak 41 software was used to fit spectra, providing both peak locations and integrations. The adventitious carbon peak in the C 1s spectrum was referenced to 284.8 eV. All peaks were fit using a Shirley baseline correction, with two constraints: i) the Gaussian:Lorentzian ratio was the same for all peaks in a given orbital, and ii) the fwhm was the same for all peaks in a given orbital.

Viscosity. Kinematic viscosities of electrolytes and electrolyte solvents (Table S1) were measured manually in an Ar-filled glovebox using a U-tube viscometer. Five repetitions were performed for each composition, with standard error <1% for all measurements. Densities of each electrolyte were measured using a micropipette and a balance to convert to dynamic viscosity.

Three-electrode electrochemical impedance spectroscopy. NMC811|Cu pouch cells were modified by inserting a Li reference electrode into each cell, such that the Li reference rests to the side of the multilayer electrode stack (so that no stack pressure was applied to the reference), prior to sealing the cells. Reference electrodes were prepared first by soldering Cu mesh onto a Ni pouch cell tab. A strip of Li metal

(for the reference) was then hammered onto the Cu mesh, and the polymer adhesive on the tab was used to seal the pouch cell after the tab was inserted into the pouch cell. Potentiostatic EIS was then performed using an Admiral Squidstat Plus1130 in the discharged state after 5 and 10 cycles at C/3 between 1.5 and 4.2 V, with 0.94 MPa of applied stack pressure on the pouch cell during the measurement. EIS was conducted at open circuit voltage from 1 MHz to 0.1 Hz, with a 10 mV excitation amplitude in three-electrode mode, using the inserted Li electrode as the reference, the Cu current collector (i.e., anode side of the battery) as the working electrode and the NMC811 cathode as the counter electrode, and then vice versa.

We did not include equivalent circuit fitting of our EIS data because the looping behavior in the HCE sample shown in Fig. 1a made it difficult to fit all of our spectra to the same equivalent circuit (regardless of which circuit we used). We could not find a circuit that was able to fit the looping behavior at all, making it impossible to extract and compare impedance-related metrics between our different conditions (i.e. electrolyte, cycle number, anode vs. cathode). Therefore, instead of reporting potentially inaccurate resistance values from imperfect fits to our data, we chose to compare the impedance values from the width of the semicircles in each spectrum, which includes both charge-transfer and SEI resistance.

3. Results

3.1. Electrochemical impedance spectroscopy of pouch cells after cycling in LHCE and HCE

We first used three-electrode electrochemical impedance spectroscopy (EIS) on Cu|NMC811 pouch cells cycled in the LHCE and HCE to ascertain the effect of BTFE on the resistance of the SEI. Inserting a separate Li metal reference electrode into the pouch cell allows us to decouple the resistances of the anode and cathode to determine where changes in impedance, if any, occur. Here, we estimate the electrode impedance (containing contributions from both interfacial and chargetransfer impedance) by measuring the width of the semicircle(s) which make up each spectrum. When examining the resistance of the Cu electrode after 5 and 10 cycles in the HCE and LHCE after discharge (i.e., after stripping Li metal from the Cu current collector), we see that in the LHCE, the Cu impedance increases from 0.70 Ω at 5 cycles to 1.15 Ω at 10 cycles (Fig. 1). Conversely, the Cu impedance only increases from $0.60~\Omega$ at 5 cycles to $0.65~\Omega$ at 10 cycles in the HCE, suggesting that the SEI formed in the LHCE either becomes thicker or more resistive at early cycle numbers. The looping behavior observed in the low frequency region of the EIS in the HCE sample is attributed to an unstable anode electrolyte interface that changes with the time constant of the EIS measurement [24].

On the cathode side, we see that there is a slight increase in impedance from 1.6 Ω after 5 cycles to 1.8 Ω after 10 cycles in the HCE, which may indicate surface reconstruction of NMC811 particles to form a resistive surface rocksalt layer [25–27] and/or changes in the interfacial chemistry of the cathode. Conversely, the impedance decreases from 1.1 Ω after 5 cycles to 0.75 Ω after 10 cycles in the LHCE (Fig. 1c and d), suggesting that CEI formation in the LHCE may mitigate this surface reconstruction process.

A comparison of the Bode plots for the LHCE and HCE samples also point toward differences in the SEI formed in the two electrolytes (Fig. S3). For example, the phase angle of the LHCE Cu after 5 and 10 cycles (Figs. S3b and d) shows an extra peak at higher frequencies (between 104 and 105 Hz) which is absent in the HCE Cu spectra (Figs. S3a and c). In addition, the phase angle of the LHCE NMC811 after 5 and 10 cycles (Figs. S3f and h) show a peak near 102–103 Hz which is absent in the HCE NMC811 spectra (Figs. S3e and g). Peaks in the phase angle of the Bode plot correspond to the capacitive impedances of unique SEI layers [28], so the extra peaks in LHCE spectra suggest that BTFE decomposition on both the anode and cathode may contribute to

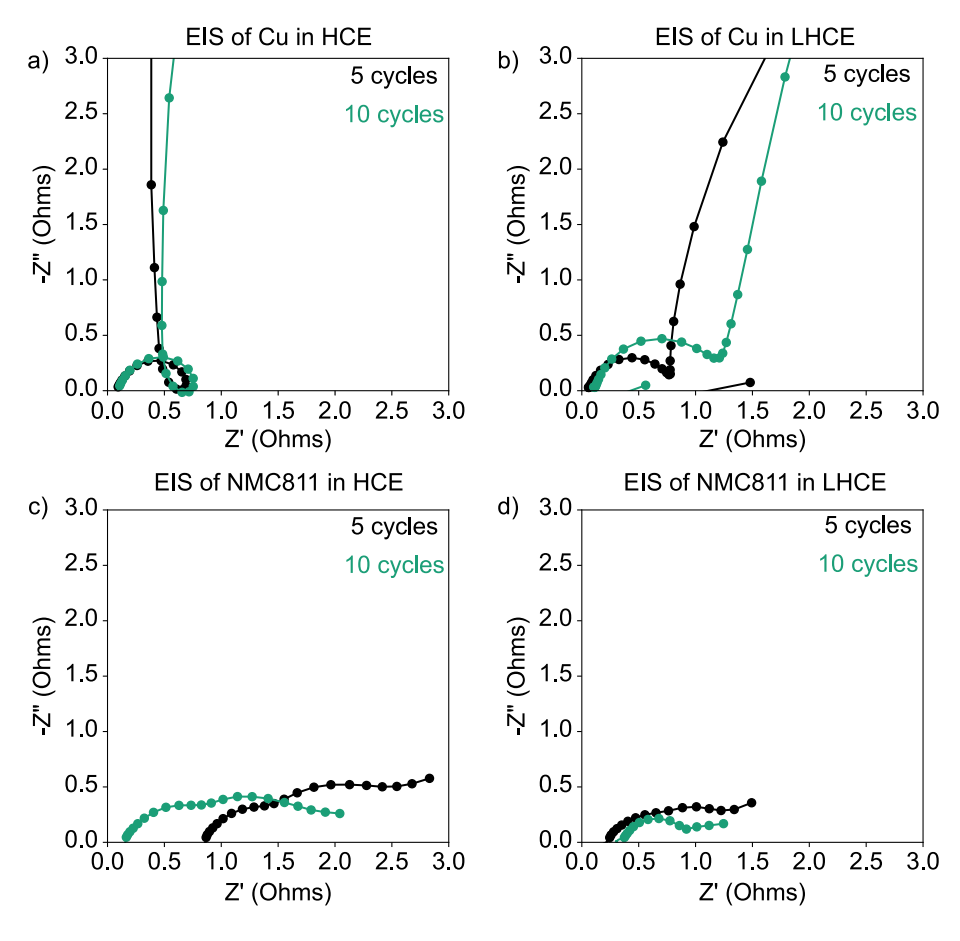


Fig. 1. Nyquist plots of three-electrode EIS where the reference electrode is Li metal of NMC811|Cu pouch cells in the HCE (a, c) and LHCE (b, d) after 5 cycles (black) and 10 cycles (green) at C/3 after discharge. In a and b, the working electrode is Cu and the counter electrode is NMC811, while in c and d, the working electrode is NMC811 and the counter electrode is Cu. Bode plots are shown in **Fig. S3**. (For interpretation of the references to colour in this figure legend, the reader is referred to the Web version of this article.)

forming distinct SEI architectures (see Section 3.3).

3.2. Diluent decomposition in LHCE during Li stripping/plating

Here, we use operando $^{19}\mathrm{F}$ NMR to simultaneously examine both LiFSI and BTFE decomposition during Li battery operation. In this experiment, we find that the amounts of FSI $^-$ and BTFE in the electrolyte solution initially decrease concurrently upon cycling (Fig. 2, bottom panel). BTFE signal intensity then appears to plateau around 20 h at \sim 17% consumption, while FSI $^-$ signal intensity decreases continuously

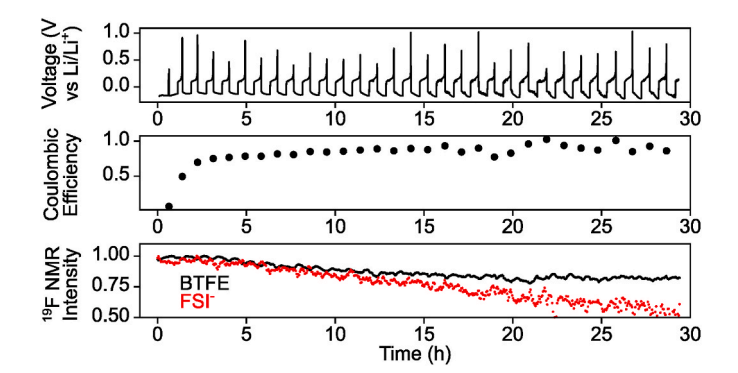


Fig. 2. Operando ¹⁹F solution NMR performed while cycling a Li|Cu cell in a NMR tube. The cell was cycled for 30 h, with each cycle comprising Li plating on Cu for 30 min at 2 mA cm $^{-2}$, followed by stripping to 1 V. The top panel shows the voltage profile vs Li/Li $^{+}$ as a function of time, and the middle panel shows the CE for each cycle. The bottom panel shows the normalized ^{19}F NMR intensity of BTFE (black) and FSI $^{-}$ (red) as a function of time. (For interpretation of the references to colour in this figure legend, the reader is referred to the Web version of this article.)

to ~45% consumption after 29 h based on their initial intensities (Fig. 2, last panel). Decomposition of both the salt and the diluent is correlated with a rapid increase in CE from 23% in the first cycle to 78% in the third cycle, fluctuating between 75% and 95% in the remaining 46 cycles. These trends suggest that decomposition of both FSI⁻ and BTFE at the Li metal surface are responsible for forming a SEI layer that promotes increased CE with cycle number and the changes in EIS observed in Fig. 1. Unfortunately, the high viscosity of the HCE (see Tables S1 and S2 and Figs. S4-S7 for viscosity and diffusion data of individual electrolytes) prohibits the collection of high resolution 19F spectra, so we instead use a low concentration electrolyte as a control (LCE) to compare electrolyte decomposition. In contrast to the LCE, no soluble species from BTFE/FSI⁻ reduction are observed during operando NMR nor ex situ NMR in the LHCE (Fig. S8), suggesting that these intermediates are short-lived before deposition in the SEI layer (N.B. NMR experiments are collected every 3 min and transient intermediates may not be captured if they are present at low concentrations). Another control experiment (¹⁹F solution NMR of a Cu electrode in the LHCE immediately after preparation, as well as 48 h after preparation) yielded no change in BTFE or FSI peak intensity (Fig. S9), indicating that the decrease in signal intensity observed in Fig. 2 does indeed come from decomposition processes that occur during Li stripping/plating.

Molecular characterization of the LHCE compared to the LCE indicates that BTFE addition has a profound effect on Li $^+$ solvation structure (Fig. S10). In particular, the effect of LiFSI addition on DMC peak width and peak position in 17 O NMR is much greater in the 1:2 DMC:BTFE (v/v) solvent than in pure DMC (Table S3 and Fig. S10), showing that Li $^+$ is much more weakly solvated in the LHCE than in the LCE, which is consistent with prior work [17]. The change in Li $^+$ solvation structure observed in the LHCE is likely due to the formation of contact-ion pairs, similar to those that form in HCEs. We attempted to analyze the HCE with 17 O NMR but were unsuccessful because high

viscosity led to peak broadening into the baseline.

When we directly compare the electrochemical performance of the LHCE versus the HCE, we see that the BTFE and FSI- decomposition observed during operando 19F NMR spectroscopy is correlated with better capacity retention in NMC811|Cu pouch cells (Fig. S11, 71% discharge (47% charge) capacity retention for LHCE and 29% discharge (8% charge) capacity retention for HCE over 14 cycles). We suspect that the improved capacity retention may be due, in part, to the lower viscosity of the LHCE that can better wet the porous NMC811 electrode than the HCE, as well as formation of a more stable SEI in the LHCE which can accommodate more stable stripping/plating processes. The initial irreversible capacity loss is also higher for the HCE than the LHCE (150 mAh g-1 vs 88 mAh g-1), suggesting that more electrolyte decomposition occurs electrochemically in the HCE as compared to the LHCE, contributing to SEI formation. BTFE decomposition products may stabilize the SEI and improve the reversibility of Li stripping/plating as compared to the HCE.

3.3. Characterization of the resulting SEI composition

To determine the composition and arrangement of the SEI formed in the LHCE, we analyzed Cu electrodes extracted from Cu|NMC811 pouch cells after cycling in the LHCE in the discharged state with XPS and magic angle spinning (MAS) solid-state NMR (SSNMR). Using $^{19}\mathrm{F}$ SSNMR, we find evidence of organic and inorganic BTFE decomposition products, as well as intact BTFE in the SEI on the anode side of the battery that was cycled in LHCE (Fig. 3, top spectrum). In this spectrum, we observe two singlets: one at -74.6 ppm and one at -79.7 ppm that are assigned to BTFE trapped in the SEI and CF $_3$ fragments, respectively. Overall, a comparison of the two spectra indicate that the SEI formed in the LHCE electrolyte is more chemically diverse (with BTFE, BTFE fragments (CF $_2$, CF $_3$), residual LiFSI, and LiF) than the one produced upon cycling in HCE (which only has LiFSI and LiF).

We next use XPS to examine both the Cu and NMC811 electrodes after cycling (Fig. S12, Table S4). F 1s spectra show that LiF and LiFSI fractions are similar in the SEI formed in the HCE and LHCE (36% and 16% respectively in the HCE, and 33% and 12% respectively in the LHCE). However, F 1s spectra of NMC811 electrodes post-cycling show that the CEI formed in the LHCE contains a larger fraction of fluorinated inorganics (45% LiF and 34% LiFSI in the LHCE, 35% LiF and 29% LiFSI in the HCE from F 1s quantification), suggesting that BTFE either decomposes or promotes anion decomposition on the cathode. We also observe a larger fraction of sulfur-containing decomposition on Cu electrodes cycled in the HCE as compared to the LHCE (13% in the LHCE vs 20% in the HCE), indicating that BTFE inclusion may suppress anion

decomposition on the anode.

We note that cells cycled in the LHCE and HCE for post mortem analysis showed differences in electrochemical performance (Fig. S11) that resulted in 15 cycles over 200 h for the LHCE and 50 cycles over 75 h for the HCE. This discrepancy in cycling times between the LHCE and HCE samples likely produced different amounts of SEI in each sample, so we made no attempt to quantify the absolute amounts of chemical compounds observed between the two samples in SSNMR. Instead, we only quantify the relative ratios of chemical species in the SEI and CEI using XPS.

Taken together, SSNMR and XPS experiments show that BTFE decomposes on the Li metal surface. $^{19}\mathrm{F}$ SSNMR of the LHCE-derived SEI indicates that BTFE, along with CF $_3$ and CF $_2$ fragments from BTFE decomposition, exist in the SEI, along with the expected byproducts from LiFSI degradation. Similarly, analysis of the surface species with XPS suggest the possible presence of BTFE decomposition species due to the presence of the C 1s XPS signal at $\sim\!289$ eV. Due to spectral overlap, the C 1s peak at $\sim\!289$ eV is assigned to both C=O and partially fluorinated carbon species, both of which are likely present in the SEI after electrochemical cycling based on SSNMR (Fig. 3). Overall, the *operando* NMR as well as post mortem SEI compositional analyses provide compelling evidence that BTFE decomposes during battery operation when using a LHCE and those byproducts of diluent decomposition may play an important role in the resulting surface chemistry.

4. Discussion

Our electrochemical and molecular characterization of NMC811 | Cu batteries cycled in the HCE and LHCE using EIS, XPS, and NMR allows us to connect impedance values to the chemical compounds that form on the surfaces of each electrode. On the Cu electrode, we observe an increase in impedance after cycling in the LHCE, while the impedance remains roughly the same in the HCE, suggesting that electrolyte decomposition in the LHCE forms a thicker or more resistive interphase (Fig. 1). Previous reports have shown that fluoroethylene carbonate (FEC) decomposition during both cycling [29] and calendar ageing [30] results in increased impedance, but that these additives improve battery performance. In addition, impedance has been shown to increase in Li| NMC811 cells using LHCEs with other diluents over 100 cycles, with improved performance [31]. We hypothesize that the CF₂- and CF₃-containing species generated from BTFE decomposition on the anode surface may alter charge-transfer kinetics and passivate the surface.

On the NMC811 electrode, we observe a slight increase in the impedance from 5 cycles to 10 cycles in the cell cycled in HCE, while a

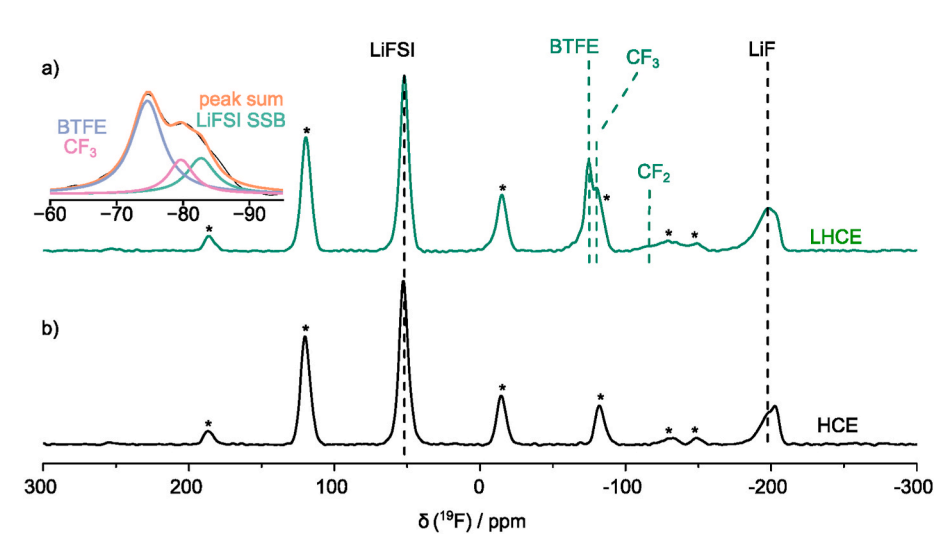


Fig. 3. ¹⁹F SSNMR spectra of the SEI formed in the LHCE after 15 cycles (a) and the HCE after 50 cycles (b) at C/10 in Cu|NMC811 pouch cells (MAS = 38 kHz). Both cells were analyzed in the discharged state. The inset shows the deconvolution of the signal observed at \sim -80 ppm into Lorentzian lineshapes representing resonances which correspond to BTFE (blue) and CF₃ fragments (pink), along with the third spinning sideband (SSBs) of LiFSI (green). Asterisks denote SSBs. (For interpretation of the references to colour in this figure legend, the reader is referred to the Web version of this article.)

decrease in impedance is observed over the same number of cycles in the LHCE. An increase in impedance is consistent with NMC811 surface reconstruction, resulting in a transition from the layered oxide structure to a rocksalt-type structure that is known to impede Li transport and reduce capacity retention [32–34]. In addition, we also observe significant swelling in the cell cycled in the HCE, which is known to result from NMC811 surface reconstruction and subsequent O₂ release from the lattice [35], and is correlated with poor cycling performance [36]. Poor electrochemical performance can also be attributed to formation of an ionically insulating or highly reactive CEI from electrolyte oxidation [25,37–39]. Thus, we believe the LHCE forms a stable CEI that protects the NMC811 from surface reconstruction and/or enables fast Li ion transport to the NMC811 particles, resulting in lower overall impedance.

Using XPS, we also find that the NMC811 electrode cycled in the LHCE has a significantly higher fraction of fluorinated compounds than NMC811 cycled in the HCE (Table S4, LiF and LiFSI), suggesting that, in the LHCE, either breakdown of BTFE or increased LiFSI decomposition/incorporation occurs on the cathode. The presence of LiF in the CEI on NMC811 has been reported previously [25,35], yet it was correlated with the formation of the rocksalt layer on the NMC811 surface [40]. Here, we see that increased LiF on the NMC811 cycled in the LHCE is correlated with lower impedance and higher capacity retention over extended cycling, suggesting that the amount and arrangement of LiF is important in controlling structure and performance in the NMC811 cathode.

5. Conclusions

Operando NMR and post-mortem compositional analysis indicates that fluorinated ether diluents are incorporated into the SEI that forms on the surface of Li metal when cycled in LHCEs. For the case of BTFE, we find that this molecule decomposes into CF₃- and CF₂-containing reaction products as well as LiF and intact BTFE that remains trapped in the porous SEI layer. Three-electrode EIS of NMC811|Cu pouch cells cycled in both the LHCE and HCE shows that the diluent-modified SEI is correlated with higher anode impedance, as well as higher overall capacity retention. These analyses lead us to reevaluate the role of highly fluorinated ether molecules in Li metal battery performance. In addition to acting as "filler" molecules that alter bulk electrolyte solvation structures, as supported by solution ¹⁷O NMR measurements, we find that diluents also contribute to SEI formation and as such, can be leveraged to tune SEI compositions and alter subsequent Li deposition behavior.

CRediT authorship contribution statement

Richard May: Conceptualization, Methodology, Investigation, Writing – original draft, Writing – review & editing. Julia C. Hestenes: Investigation, Methodology, Writing – review & editing. Naiara A. Munich: Investigation, Writing – review & editing. Lauren E. Marbella: Conceptualization, Methodology, Writing – original draft, Supervision, Funding acquisition, Writing – review & editing.

Declaration of competing interest

The authors declare that they have no known competing financial interests or personal relationships that could have appeared to influence the work reported in this paper.

Data availability

Data will be made available on request.

Acknowledgments

This work was supported, in part, by National Science Foundation

CAREER Award (CBET-2045262). A portion of this work was supported by the Research Corporation for Science Advancement through a Cottrell Scholar Award (28206). Richard May is supported by the U.S. Department of Defense through the National Defense Science & Engineering Graduate (NDSEG) Fellowship program. Julia C. Hestenes is supported by the National Science Foundation through the Graduate Research Fellowship Program (NSF GRFP #2021278071). N.M. was supported by the Science Pathways Scholars Program of Barnard College of Columbia University.

Appendix A. Supplementary data

Supplementary data to this article can be found online at https://doi.org/10.1016/j.jpowsour.2022.232299.

References

- [1] E. Peled, S. Menkin, J. Electrochem. Soc. 164 (2017) A1703.
- [2] X.B. Cheng, R. Zhang, C.Z. Zhao, F. Wei, J.G. Zhang, Q. Zhang, Adv. Sci. 3 (2015) 1–20
- [3] D. Aurbach, J. Power Sources 89 (2000) 206-218.
- [4] A.J. Ilott, A. Jerschow, J. Phys. Chem. C 122 (2018) 12598-12604.
- [5] C. Fang, X. Wang, Y.S. Meng, Trends Chem. 1 (2019) 152-158.
- [6] O. Borodin, J. Self, K.A. Persson, C. Wang, K. Xu, Joule 4 (2020) 69-100.
- [7] Y. Yamada, A. Yamada, J. Electrochem. Soc. 162 (2015) A2406.
- [8] S.K. Jeong, H.Y. Seo, D.H. Kim, H.K. Han, J.G. Kim, Y.B. Lee, Y. Iriyama, T. Abe, Z. Ogumi, Electrochem. Commun. 10 (2008) 635–638.
- [9] L. Suo, O. Borodin, T. Gao, M. Olguin, J. Ho, X. Fan, C. Luo, C. Wang, K. Xu, Science 350 (1979) 938–943, 2015.
- [10] C.A. Angell, C. Liu, E. Sanchez, Nature 362 (1993) 137-139.
- [11] Y. Yamada, K. Furukawa, K. Sodeyama, K. Kikuchi, M. Yaegashi, Y. Tateyama, A. Yamada, J. Am. Chem. Soc. 136 (2014) 5039–5046.
- [12] M. Winter, B. Barnett, K. Xu, Chem. Rev. 118 (2018) 11433-11456.
- [13] J.B. Goodenough, Y. Kim, Chem. Mater. 22 (2010) 587–603.
- [14] Y. Zheng, F.A. Soto, V. Ponce, J.M. Seminario, X. Cao, J.G. Zhang, P.B. Balbuena, Int. J. Mater. Chem. A 7 (2019) 25047–25055.
- [15] Y. Zheng, P.B. Balbuena, J. Chem. Phys. 154 (2021), 104702.
- [16] J. Qian, W.A. Henderson, W. Xu, P. Bhattacharya, M. Engelhard, O. Borodin, J. G. Zhang, Nat. Commun. 6 (2015) 6362.
- [17] X. Ren, S. Chen, H. Lee, D. Mei, M.H. Engelhard, S.D. Burton, W. Zhao, J. Zheng, Q. Li, M.S. Ding, M. Schroeder, J. Alvarado, K. Xu, Y.S. Meng, J. Liu, J.G. Zhang, W. Xu, Chem 4 (2018) 1–16.
- [18] S. Chen, J. Zheng, D. Mei, K.S. Han, M.H. Engelhard, W. Zhao, W. Xu, J. Liu, J. G. Zhang, Adv. Mater. 30 (2018), 1706102.
- [19] X. Cao, H. Jia, W. Xu, J.-G. Zhang, J. Electrochem. Soc. 168 (2021), 010522.
- [20] X. Ren, L. Zou, X. Cao, M.H. Engelhard, W. Liu, S.D. Burton, H. Lee, C. Niu, B. E. Matthews, Z. Zhu, C. Wang, B.W. Arey, J. Xiao, J. Liu, J.G. Zhang, W. Xu, Joule 3 (2019) 1662–1676.
- [21] J.J. Helmus, C.P. Jaroniec, J. Biomol. NMR 55 (2013) 355-367.
- [22] M. Newville, A. Ingargiola, T. Stensitzki and D. B. Allen, Zenodo, DOI:10.5281/ ZENODO.11813.
- [23] P.M. Aguiar, J.F. Jacquinot, D. Sakellariou, J. Magn. Reson. 200 (2009) 6-14.
- [24] W. Chang, R. May, M. Wang, G. Thorsteinsson, J. Sakamoto, L. Marbella, D. Steingart, Nat. Commun. 12 (2021) 1–12.
- [25] J.C. Hestenes, R. May, J.T. Sadowski, N. Munich, L.E. Marbella, Chem. Mater. 34 (2021) 232–243.
- [26] Y. Yu, P. Karayaylali, L. Giordano, J. Corchado-Garciá, J. Hwang, D. Sokaras, F. Maglia, R. Jung, F.S. Gittleson, Y. Shao-Horn, ACS Appl. Mater. Interfaces 12 (2020) 55865–55875.
- [27] F. Lin, I.M. Markus, D. Nordlund, T.C. Weng, M.D. Asta, H.L. Xin, M.M. Doeff, Nat. Commun. 5 (2014) 1–9.
- [28] F.M. Wang, J. Rick, Solid State Ionics 268 (2014) 31–34.
- [29] J.-H. Song, J.-T. Yeon, J.-Y. Jang, J.-G. Han, S.-M. Lee, N.-S. Choi, J. Electrochem. Soc. 160 (2013) A873–A881.
- [30] Z.L. Brown, S. Jurng, C.C. Nguyen, B.L. Lucht, ACS Appl. Energy Mater. 1 (2018) 3057–3062.
- [31] X. Cao, L. Zou, B.E. Matthews, L. Zhang, X. He, X. Ren, M.H. Engelhard, S. D. Burton, P.Z. El-Khoury, H.-S. Lim, C. Niu, H. Lee, C. Wang, B.W. Arey, C. Wang, J. Xiao, J. Liu, W. Xu, J.-G. Zhang, Energy Storage Mater. 34 (2021) 76–84.
- [32] D.P. Abraham, J.L. Knuth, D.W. Dees, I. Bloom, J.P. Christophersen, J. Power Sources 170 (2007) 465–475.
- [33] J.H. Kim, S.J. Kim, T. Yuk, J. Kim, C.S. Yoon, Y.K. Sun, ACS Energy Lett. 3 (2018) 3002–3007.
- [34] M. Gu, I. Belharouak, J. Zheng, H. Wu, J. Xiao, A. Genc, K. Amine, S. Thevuthasan, D.R. Baer, J.G. Zhang, N.D. Browning, J. Liu, C. Wang, ACS Nano 7 (2013) 760–767.
- [35] A.O. Kondrakov, H. Geßwein, K. Galdina, L. de Biasi, V. Meded, E.O. Filatova, G. Schumacher, W. Wenzel, P. Hartmann, T. Brezesinski, J. Janek, J. Phys. Chem. C. 121 (2017) 24381–24388.
- [36] R. Jung, M. Metzger, F. Maglia, C. Stinner, H.A. Gasteiger, J. Electrochem. Soc. 164 (2017) A1361.

- [37] Yirui Zhang, Yu Katayama, Ryoichi Tatara, Livia Giordano, Yu Yang, Dimitrios Fraggedakis, J. Guangwen Sun, Filippo Maglia, M.Z. Roland Jung, Bazant and Yang Shao-Horn, Energy Environ. Sci. 13 (2020) 183–199.
 [38] Y. Yu, P. Karayaylali, Y. Katayama, L. Giordano, M. Gauthier, F. Maglia, R. Jung, I. Lund, Y. Shao-Horn, J. Phys. Chem. C 122 (2018) 27368–27382.
- [39] B.L.D. Rinkel, D.S. Hall, I. Temprano, C.P. Grey, J. Am. Chem. Soc. 142 (2020) 15058-15074.
- [40] F. Lin, I.M. Markus, D. Nordlund, T.C. Weng, M.D. Asta, H.L. Xin, M.M. Doeff, Nat. Commun. 5 (2014) 1–9, 2014 5:1.